RESEARCH ARTICLE

Variable band-gap Sr-hexagonal ferrites on carboxylated graphene oxide composite as an efficient photocatalytic semiconductor

Masomeh Taghipour[1], Mohammad Yousefi[2], Reza Fazaeli[3,*], Masoud Darvish Ganji[4]

[1] Department of Chemistry, Science and Research Branch, Islamic Azad University, Tehran, Iran

[2] Department of Chemistry, Yadegar-e Imam Khomeyni (RAH) Shar-e Rey Branch, Islamic Azad University, Tehran, Iran

[3] Department of Chemistry, South Tehran Branch, Islamic Azad University, Tehran, Iran

[4] Department of Chemistry, Qaemshahr Branch, Islamic Azad University, Qaemshahr, Iran

ARTICLE INFO

Article History:
Received 2021-11-29
Accepted 2022-02-22
Published 2022-09-30

Keywords:
M-type hexagonalferrite,
Functionalized graphene oxide,
Photodegradation,
Enrofeloxacin

ABSTRACT

In this study, Sr Gd_x $Fe_{(12-x)}$ O_{19} nanostructures (x= 0, 0.2(3% Gd), 0.4 (6%Gd),0.6(9%Gd), 0.8 (12%Gd)) were synthesized by self-combustion sol-gel method and then calcined at the temperature of for 3 h. This compound was then composited with functionalized graphene oxide (GO) for the photocatalytic degradation of Enrofeloxacin. FE-SEM, EDS, XRD, and FT-IR analysis were employed to investigate the particle size, elemental composition, morphological structure, functional groups determination and structural composition of the samples. VSM, BET-BJH, TGA-DTA, DRS and zeta potential analysis were also used to assess the magnetic properties, surface area, thermal stability, band-gap determination and suspension stability of the specimens, respectively. For evaluation of performance, photocatalytic degradation of Enrofeloxacin (an antibiotic that is widely used for domestic animals) is performed. The results showed that the 3% and 6% Gd-doped composites had the highest efficiencies in the photocatalytic reaction.

How to cite this article
Taghipour M., Yousefi M., Fazaeli R., Darvish Ganji M., Variable band-gap Sr-hexagonal ferrites on carboxylated graphene oxide composite as an efficient photocatalytic semiconductor. J. Nanoanalysis., 2022; 9(3): 193-205. DOI: 10.22034/jna.2022.1946189.1281

INTRODUCTION

Recent progress in the industries and technologies has resulted in a huge amount of wastewater that needs to be treated before entering the environment. Due to their toxicity, organic pollutants in the aqueous solutions can be seriously hazardous even at low concentrations. The resistance of micro-pollutants (especially antibiotics) is of crucial significance in the aqueous matrices as these compounds are widely used in humans and animals as well as poultry [1]. Wastewater treatment plants (WWTP) fail to eliminate the antibiotics effectively and these compounds have been detected in biological matrices all around the world. They can be found in various concentrations: several µg/l in hospital and urban effluents to several ng/l in surface waters, seawater, and underground water [2]. Enrofloxacin (ENR) and Pefloxacin (PEF) belong to the Fluoroquinolone (FQ) class and are among the newly-emerged pollutants [3]. Antibiotics inhibit the bacterial division but they do not completely eliminate them; thus they cannot be eliminated by conventional biological wastewater treatment plants. Finding an efficient and cost-effective method for the elimination of antibiotics from water sources is highly demanded [4-5]. Advanced oxidation processes (AOP), in particular, photocatalysis and photochemistry are among the superior technologies which can eliminate these resistant pollutants [6].

Recent decades have witnessed the use of

* Corresponding Author Email: *r_fazaeli@azad.ac.ir*

magnetic nanomaterials for adsorption and degradation of the pollutants [7]. Among these magnetic nanomaterials, Fe_2O_3, ferrites (MFe_2O_4, M=Co, Ni, Zn), and hexagonal ferrites ($MFe_{12}O_{19}$ M=Sr, Ba, Pb, Cu) have exhibited effective pollutant removal from wastewater [8-11].

Hexagonal ferrites are a group of magnetic oxides known as magnetoplumbite with hexagonal structure. These materials have low density, strong adsorption, and thin thickness [12]. Hexagonalferrites (especially strontium hexagonalferrite) are hard magnetic matters which have been used in composites due to their mechanical and chemical stability as well as corrosion resistivity. These materials not only result in composites with magnetic properties, but they can promote better features for pollution adsorption processes [13]. The majority of the studies on strontium hexagonalferrite are focused on microwave absorption [14-15].

In addition to microwave absorption, photocatalytic degradation by magnetic nanoferrites has also been addressed [20-22]. The magnetic properties of hexagonalferrites could be improved by surface modification through doping [23-32]. Among the substituted metals, a few studies have addressed the surface modification of magnetoplumbite with Gd [33-35]. As an effective adsorbent for various pollutants, graphene oxide is among the proper carbon-based compounds for compositing with hexagonalferrites, according to the researcher. Graphene is a single-layer or multi-layer honeycomb structure of 2-D sheets with sp^2 hybridization. Owing to its low weight, high specific area, superior mechanical strength, excellent dielectric features, and high aspect ratio this structure is a suitable candidate for the conductive networks [36-37].

In this research, strontium hexagonalferrite doped with different levels of Gd was synthesized on a graphene oxide support and its features were characterized. Finally, some performance tests were done to evaluate the effect of gadolinium doping on photocatalytic efficiency.

EXPERIMENTAL

Materials

Following chemicals were employed to synthesize the Gd-doped strontium ferrite and its stabilization on the functionalized graphene oxide:strontium nitrate ($Sr(NO_3)_2$) 98%, iron nitrate nonhydrated ($Fe(NO_3)_3.9H_2O$) 98%, Gadolinium(III) nitrate hexahydrate ($Gd(NO_3).6H_2O$ 98%,Ammonium solution,(NH_4OH), Citric acid ($C_6H_8O_7.H_2O$) Dithioxamide ($NH_2CSCSNH_2$), and functionalized graphene oxide carboxyl were supplied by Merck. Erofeloxacin oral solution 10% was supplied by Damyaran Company. All the reagents used were of analytical grade and were used as bought without any further purification.

Synthesis

Synthesis of Sr $Gd_xFe_{12-x}O_{19}$

Sr $Gd_xFe_{12-x}O_{19}$/GO-COOH was synthesized by the self-combustion sol-gel method. In a typical procedure, a suitable amount of iron nitrate, strontium nitrate, citric acid (as fuel), and gadolinium nitrate were weighed. The molar ratio of citric acid to salts was set at 1.5:1. First, citric acid was dissolved in 100 mL deionized water. Then the other cations were added (from low to high amounts) to the solution with 20-minute intervals and stirred at 80 °C for 3 h. Ammonium was dropwise added to the solution to set the solution pH at 7. By gradual increase of the temperature to 120 °C, the solution converted into a gel and self-combustion occurred by temperature enhancement to 200 °C giving rise to a gray powder. The obtained powder was first milled and then calcined for 2 h at 550 °C followed by sintering at 1050 °C for 4 h in an electrical furnace (compound 1).

Synthesis of Sr $Gd_xFe_{12-x}O_{19}$/GO-COOH

25 ml ethanol was added to a suitable amount of functionalized graphene oxide and sonicated for 1 h. Then, some dithiooxamide (DTOx) ligand was added to compound 1 and sonicated for 1 h. Afterward, Sr $Gd_xFe_{12-x}O_{19}$ was added to this solution at a molar ratio of 1:1 and sonicated for 2 h followed by one-hour oven-drying at 60 °C.

Characterization

The crystallite properties of the prepared samples were characterized by X-ray Diffractometer (X' Pert Pro, Pan analytical) with Cu Kα source using CuKα line radiation at 2θ range of 20-80 ° with the step size of 0.02°.

Furrier Transform Infrared (FT-IR, Perkin Elmer Spectrum 65) spectroscopy was also applied to examine the chemical structure of the samples.

The surface morphology was determined by Field Emission Scanning Electron Microscopy (FE-SEM, ZIES, and VP-500) equipped with energy dispersive X-ray (EDX) analysis.

M-H curves of magnetic products were obtained using Vibrating Sample Magnetometer (VSM Daghigh Kavir Company LBKFB model-Meghnatis) at room temperature.

Differential thermal analysis DTA and Thermal gravimetric analysis TGA (Rheometric Scientific STA 1500) were applied in Ar atmosphere at a heating rate of 10deg/min between 25 and 800 °C.

Surface area and pore size distribution were measured by the Brunauer-Emmett-Teller (BET) analyzer (Microtrac Bel Corp BElSORP Mini). Diffuse reflectance spectra (DRS Shimadzu UV 2550.) of the ferrite nanoparticles were recorded as well. Zeta potential was also applied to evaluate the stability of the colloidal solution of the compounds and analyze the Enrofeloxacin.

Catalytic experimental procedure

The photocatalytic properties of the synthesized materials in the degradation of ENR were assessed in 5 concentrations (C_1= 2.4 $\times10^{-3}$, C_2= 1.44 $\times10^{-3}$, C_3= 1.92 $\times10^{-3}$, C_4= 3$\times10^{-3}$, and C_5= 4.5 $\times10^{-3}$ g/L).

The degradation efficiency was calculated by the following equation:

$$\text{Efficiency\%} = \frac{(C_0 - C_f)}{C_0} \times 100 \qquad \text{Eq. 1}$$

In which C_0 and C_f are the initial and final ENR concentrations, respectively.

RESULTS AND DISCUSSIONS

XRD pattern analysis

The XRD pattern of the strontium hexagonalferrite with the chemical formula of $SrFe_{12}O_{19,}$ Gd=0 matched with 1207-024-00 pdf card. The special group of the samples was p/63mmc with a hexagonal structure (Fig. 1).

The cell volume and the lattice parameters were calculated from the equation:

$$\frac{1}{d^2} = \frac{4}{3}\left(\frac{h^2 + hk + k^2}{a^2}\right) + \frac{l^2}{c^2} \qquad \text{Eq.2}$$

Where d is the crystal plane distance. a and c are lattice parameters, h, k and l are Miller indices. In comparison, the radius of Gd^{3+} (1.07Å) is larger than Fe^{3+} (0.63Å). The lattic parameters (from XRD), average particle size (from SEM) and Cell volum of Sr Gd_x $Fe_{(12-x)}$ O_{19} , (X=0, 3%, 6%, 9%, 12%) are shown in Table 1.

With notice to the XRD data, the crystallite sizes are computed using Willamson-Hall equation and reported in Table 3.

Calcination at 1050 °C resulted in the formation of pure strontium hexagonal ferrite. Two groups of peaks can be observed in these patterns: the first group is related to undoped Gd or the pure state which can be seen in all the patterns. The second group is associated with the doped Gd which peaks show slight shifts. The peaks distance got more evident in SrMGd (3%). At 2θ=47.5°, this

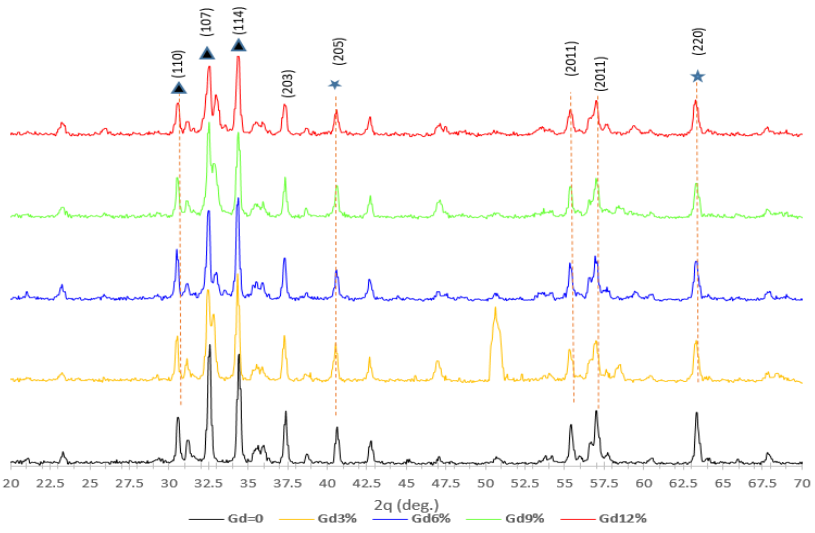

Fig. 1 . Diffraction patterns for $SrGd_xFe_{(12-x)}O_{19}$/GO-COOH for different amount (%) of Gd.

Table 1. Lattic parameters, Cell volume and crystal size of ferrites composite ($SrGd_xFe_{12-x}O_{19}$/GO-COOH).

Compound	(c/a)	V (Å^3)	Avg. particle Size (nm)
SrM/ fGO	3.906	686.43	112
SrMGd 3% / fGO	3.914	689.83	97.65
SrMGd 6 % / fGO	3.914	689.88	62.99
SrMGd 9 % / fGO	3.906	686.49	81.86
SrMGd 12 % / fGO	3.906	686.43	38.33

Table 2 Bandgap values of the synthesized structu

Sample	E_g (eV)
Sr M	3.01
Sr GdM (%3)	2.02
Sr GdM (%6)	2.14
Sr GdM (%9)	3.16
Sr GdM (%12)	2.8
SrM/GO	3.7

Table 3. The calculated crystallite size of the synthesized compounds based on diffraction data.

Sample	crystallite Size (nm)
Sr M/ GO	56.05
SrM Gd /Go (%3)	31.52
SrM Gd /Go (%6)	30.22
SrM Gd /Go (%9)	18.37
SrM Gd /Go (%12)	48.33

peak shifted toward smaller angles while the shift was toward higher angles in the other Gd-doped strontium ferrite samples. All the structures exhibited a distinct peak at $2\theta=51^0$ indicating tangible changes in the crystalline plane. Due to the low dosage of Gd, it can be inferred; it possibly diffused in the lattice and formed a pure crystal plane.

FT-IR studies

FT-IR technique has been employed to identify the functional groups and structural features of the synthesized composites (Fig. 2). In M-type hexagonals, two groups of absorption bands can be observed in 430-590 cm^{-1} which is associated with the stretching vibrations. In 435 cm^{-1}, the variations in the intensities of the peak are in line with the Gd doping. This region can be thus employed for quantifying the amount of Gd doping. The high-frequency band in the range of 590 cm^{-1} can be assigned to tetrahedral sites while the lower frequencies can be ascribed to octahedral sites. The absorption band corresponds to the stretching vibration due to reactions between oxygen and cations in the octahedral and tetrahedral sites. The vibrational modes of tetrahedral clusters are higher than those of the octahedral ones which can be attributed to the shorter bond length. A broad absorption can be observed in wavenumbers below 380 cm^{-1} which can be due to Fe-O stretching vibrations. By increasing the amount of Gd, the absorption frequencies shifted to smaller wavenumbers which can be assigned to the higher atomic mass of Gd in comparing with Fe.

Determination of bandgap energy by DRS

Using DRS analysis and Kubelka-Munk equation (Eq. 3), the bandgap of the SrM samples was determined. This method addresses the interactions between the incident light and the surface layer of the studied sample. F is the Kubelka-Munk function; while R denotes the reflection. Fig. 3 and Table 2 show the bandgap of the synthesized structures.

$$F(R)=(1-R^2)/2R \qquad \text{Eq. 3}$$

No strictly ascending/descending trend was

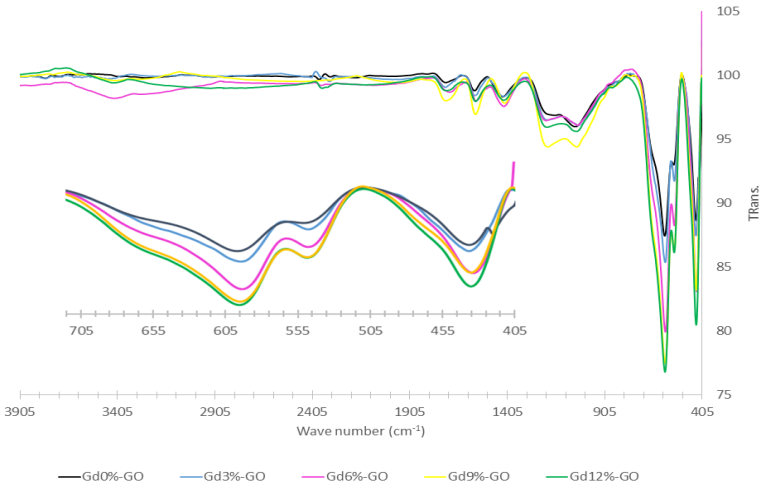

Fig. 2. FTIR spectra of Sr $Gd_xFe_{12-x}O_{19}$/GO-COOH samples

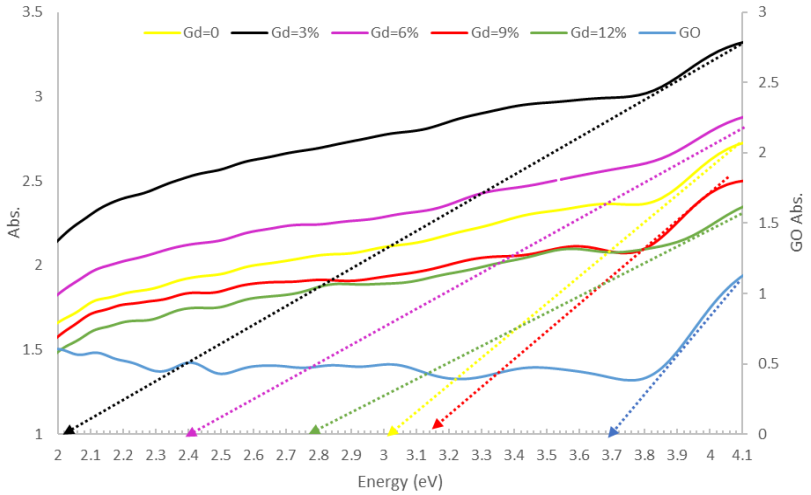

Fig. 3. Bandgap of strontium ferrite compounds

observed in the obtained data. The decline of the conduction band however, showed some dependence on the dopant content, and the lowest conduction bands were determined in SrMGd(3%) and SrMGd (6%) samples. Therefore, the best photocatalytic features are anticipated in these samples. The bandgap decreased by increasing the dopant content; thus it can be concluded that by increasing the concentration, the repulsion rose and the inter-layer distance grew. The layered structure of ferrites in SrMGd(3%) and SrMGd(6%) was in a way that the atoms had the best interaction. Owing to its empty orbitals, Gd lowered the conduction band and acted as a p-type dopant

FE-SEM Analysis

According to FE-SEM images, the M-type strontium hexaferrite particles are hexagonal with uniform particle size distribution (Fig 4). Table 3 also lists the mean size of the particles. In the graphene-composited samples, the density of the particles on the graphene oxide surface declined with increasing the dopant content which hindered the accumulation of the particles and thus their size enlargement. Regarding the different mass fractions of iron and gadolinium nitrates used in production of the samples, the molecular formula of the formed ferrite (qualitatively determined by EDXA) is in good agreement with the proposed formulas. The EDXA results are, however, smaller

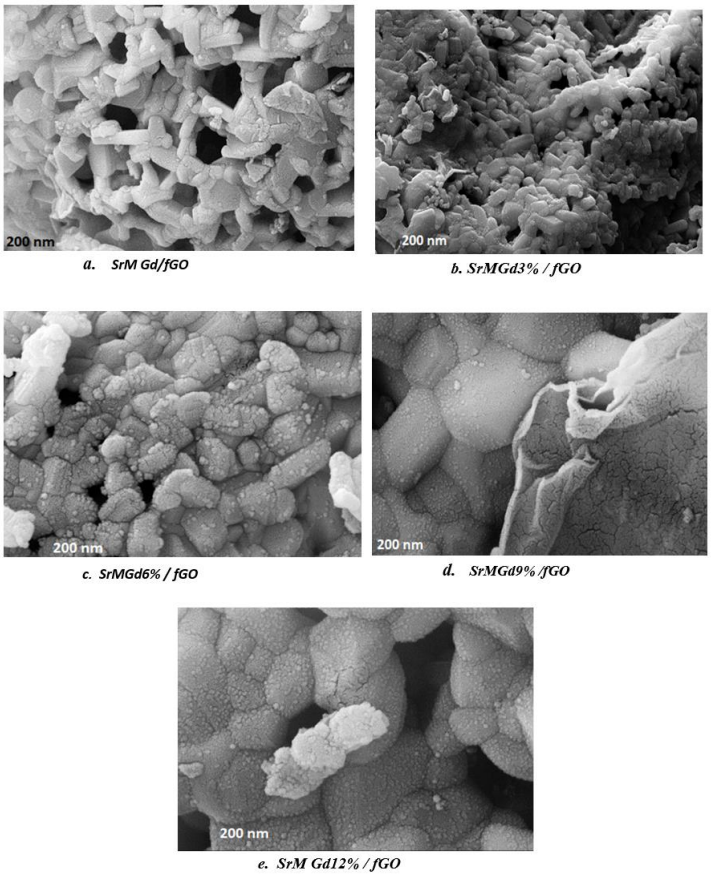

Fig. 4. FESEM images of the synthesized ferrites along with their EDXA results

Table 4. Molecular formula and the weight percentage of the doped atom.

Mass(g) used for synthesis		Nominated atomic x	Nominated wt%	EDXA wt%	Abbreviated
$Fe(NO3)_3$,9 (H_2O)	Gd ($NO3)_3$	$Sr.Gd_xFe_{12-x}O_{19}$	Gd%	Gd%	Name
11.2	0.8	0.93	12.63	10.9	Gd 12
11.4	0.6	0.69	9.57	8.5	Gd 9
11.6	0.4	0.46	6.51	5.1	Gd 6
11.8	0.2	0.23	3.33	2.8	Gd 3
12	0	0	0	0	Gd 0

than the XRD-determined values which could be explained by the possibility of incomplete reaction and wasted materials. These values are listed in Table 4.

VSM studies

The magnetic properties of the samples were assessed by measuring their hysteresis at room temperature using a VSM apparatus. The remnants magnetization (M_r), saturation magnetization (M_s), coercivity (Hc) and squareness ratio were obtained from the hysteresis loops and as presented in Fig. 5 and Table 5. By substitution of Fe with Gd, the coercivity force declined compared to the pure sample. The reduction in the coercivity force (H_c) in the doped samples can be assigned to decline magnetocrystalline anisotropy and ease of the magnetization direction deviation from the C axis in the hexagonal structure of strontium hexagonalferrite toward its base-parallel plane. In general, the up-spin iron ions are placed in octahedral (2a, 12K) and by-pyramided (2b) sites; while the down-spin Fe ions can be found in tetrahedral ($4f_1$) and octahedral ($4f_2$) sites of the

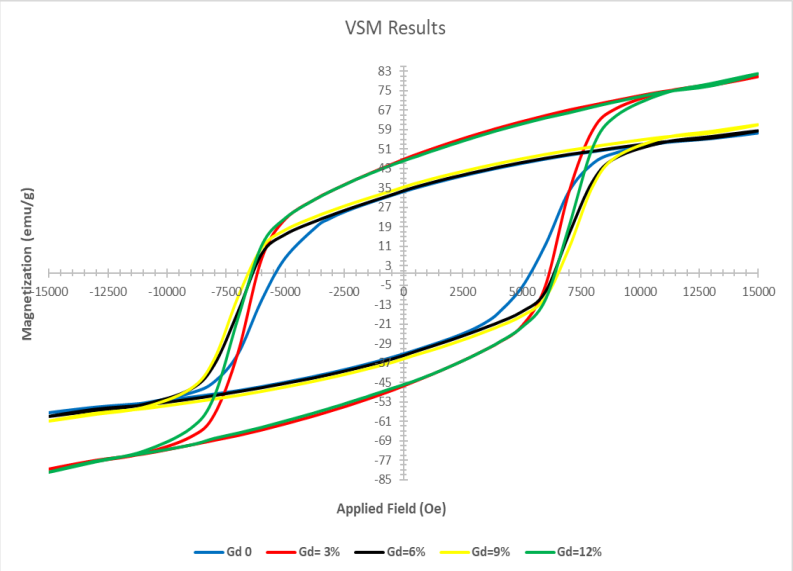

Fig. 5. Magnetic measurements curve of the synthesized compound

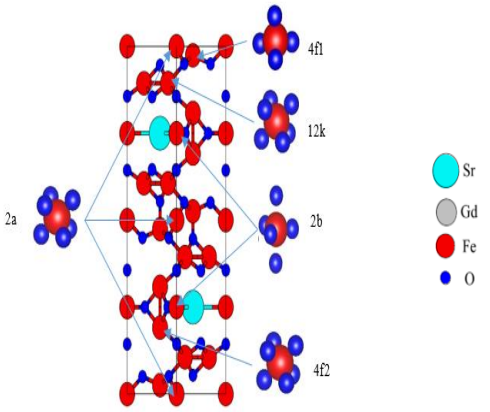

Fig. 6. Atomic arrangement in the Gd-doped strontium hexaferrite.

Table 5. M_r, M_s, and H_c of the samples.

Sample	M_r (emu/g)	M_s (emu/g)	M_r/M	$\|H_c(O_e)\|$
SrM	33	55	0.6	4900
Sr GdM (%3)	47	58	0.8	6100
Sr GdM (%6)	34	56	0.6	6500
Sr GdM (%9)	35	76	0.4	6600
Sr GdM (%12)	46	77	0.5	6500

strontium hexagonalferrite (Fig. 6). Among 12 Fe^{3+} ions, 8 are up-spin and placed in 2a, 12K, and 2b, and 4 (down-spin) were situated in 4f1 and $4f_2$. Therefore, three parallel (2a, 12K, and 2b) and 2 anti-parallels ($4f_1$ and $4f_2$) sub-lattices were formed which, by exchange-correlation with C^{2-} ions, resulted in ferrimagnetic structure [38-40].

BET/BJH Analysis

BET analysis was employed to study the effective surface of the Gd-doped strontium hexagonal ferrites and their composite with graphene oxide based on the volume of the adsorbed/desorbed N_2 gas at a constant temperature. After placing the sample in the liquid nitrogen tank, the amount of the adsorbed gas was calculated at each stage by a

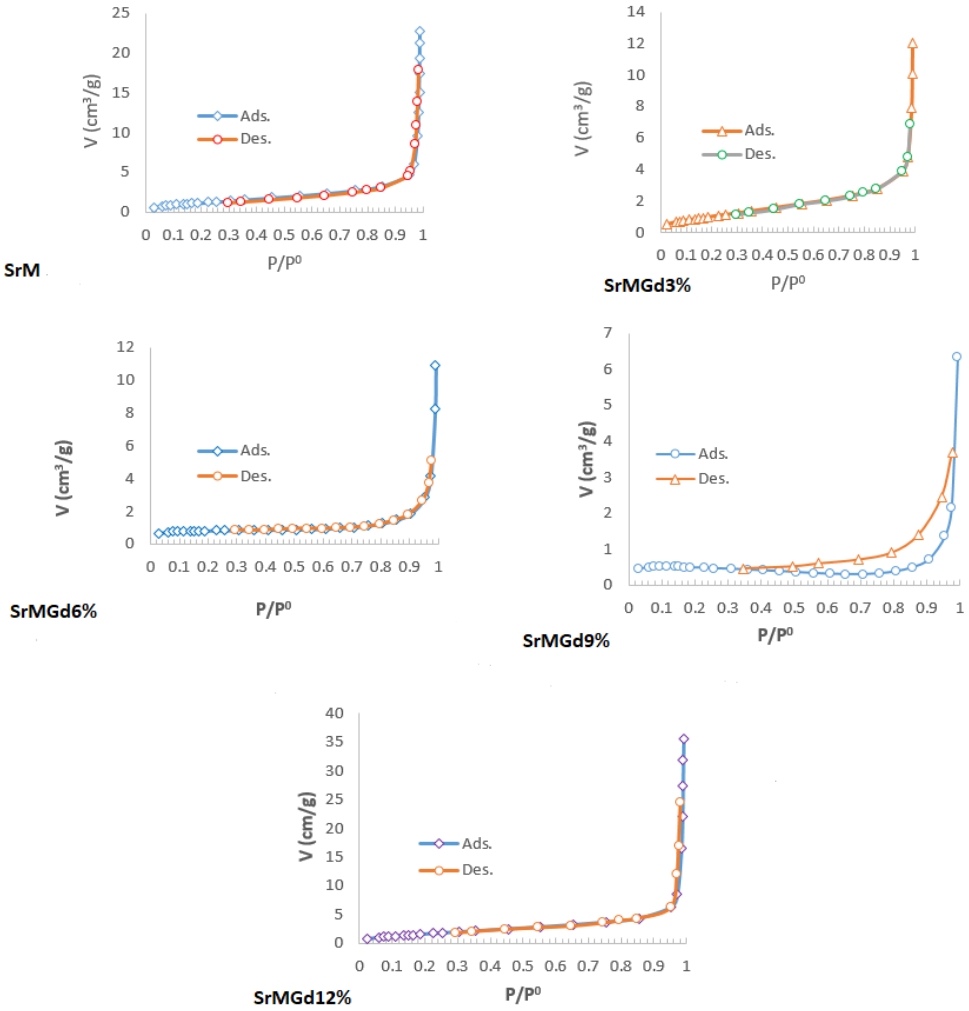

Fig. 7. adsorption/desorption curves of the synthesized samples

gradual increase of the N_2 gas pressure. Desorption was also assessed by a gradual decrease in the N_2 pressure at a constant temperature. This system operates based on the Brunauer-Emmett-Teller (BET) theory. As can be seen in Fig. 7, the isotherm plot for all composites follows a standard type IV isotherm, which is the characteristic of mesoporous materials. Initially, at a relative pressure less than 0.05, a sudden rise occurs in adsorption, which is related to the monolayer adsorption on the surface of the composites. On the other hand, at higher relative pressures of about 0.6, nitrogen adsorption occurs as multilayer adsorption, resulting a further growth in gas adsorption near the relative saturation pressure (P/P_0=1), thereby enhancing the adsorption and capillary condensation between the Sr ferrites composite in the large cavities. All the patterns of meso-porous material are related to the type IV isotherm. Furthermore, specific area (as) obtained from BET and Langmuir methods, the volume required to cover one layer of the surface (Vm), adsorption heat constant (C), pore area (ap), mean pore radium (rp) and mean pore volume (Vp) were calculated and reported in Table 6 for all the synthesized samples. The results suggest that after Gd doping (3%) in Sr/M, the surface area increased from 4.5708 to 5.2247 (m2/g); however, by the further increase of Gd content (6%, 9%, and 12%), the surface area declined. Similarly, upon Gd doping in SrM/GO, the surface area increased from 4.7167 to 5.8916 (m2/g); however, by a further increase of Gd content (6%, 9% and 12%), the surface area reduced. Moreover, an increase in GO content of the catalyst enhanced its surface area. Among the tested catalysts, SrMGd (3%) and SrMGd (6%)/GO exhibited the highest chemical adsorptions (290.93

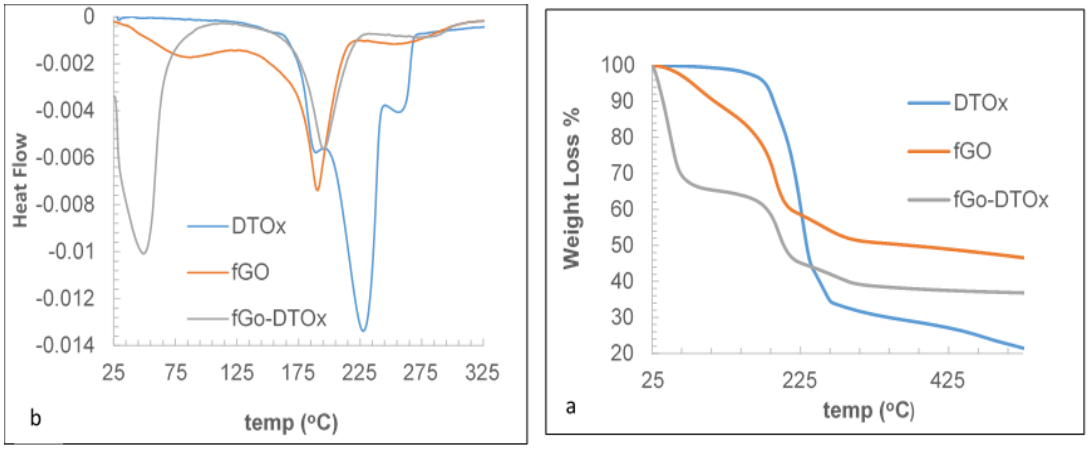

Fig. 8 . (a) DTA and (b) TGA pattern of DTOx, f-GO,f-GO/DTOx

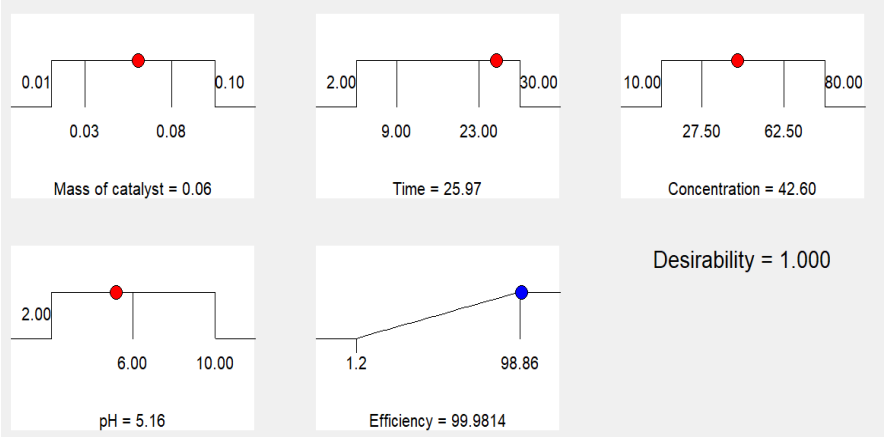

Fig. 9. Optimization of the operational parameters

and 365.53 mg/g, respectively). It can be concluded that the adsorbates were well adsorbed by the catalyst giving rise to enhanced photocatalytic degradation. On the other hand, GO-containing catalysts possessed higher chemical adsorption as compared to their GO-free counterparts. Based on Table 6, by doping Gd to SrM and SrM/GO with various weight percentages, the total pore volume decreased implying proper doping of Gd in SrM and SrM/GO structures.

If there is a significant distance between adsorption and desorption branches observed, it means that there is a significant difference between neck radius and body radius of pores exist. So, it can be concluded that in Gd(9%),probably the pores have a shape like ink-bottle.

Thermal studies (DTA- TGA)

Fig. 8 illustrates the DTA and TGA patterns of the specimens. In the TGA pattern of dithiooxamide (DTOx) as a ligand, a considerable weight loss can be observed at 220 °C which can be assigned to simultaneous thermal decomposition and sublimation. Two breaks can be found in the pattern of the GO-OH in 170 and 220 °Cwhich can be ascribed to decarboxylation and decomposition of the carbonaceous structure. In the case of DTOx-functionalized GO, three breaks can be detected at 50, 200, and 275 °C which can be attributed to the peptide groups due to DTOx reaction with graphene-attached COOH, decomposition of graphene oxide structure, and the endothermic thermal decomposition and decarboxylation, respectively. The DTA pattern confirmed the TGA patterns.

Zeta Potential Analysis

The zeta potential is an indication of the surface potential, and determines the magnitude of the electrical double layer repulsion. The total

Table 6. BET/BJH parameters of strontium hexagonalferrite compound.

Compound	$a_{S,BET}$ (m^2/g)	$a_{S,Lang.}$ (m^2/g)	V_m (cm^3/g)	C	a_P (m^2/g)	r_P (nm)	V_P (cm^3/g)
Sr M/GO	4.1167	5.1536	1.1841	294.73	1.1276	12.2	0.0295
Sr M Gd (%3)/GO	3.2916	3.8693	0.8890	152.53	0.3846	12.2	0.0207
Sr M Gd (%6)/GO	3.1358	4.0363	0.9274	116.46	2.2111	10.65	0.0201
Sr M Gd (%9)/GO	4.6854	6.4579	1.4837	92.51	4.1055	1.22	0.0266
Sr M Gd (%12)/GO	5.4687	7.3000	1.6772	137.06	4.3948	10.65	0.0342

Table 7. Zeta potential variation with pH.

Zeta Potential (mV)	pH
19	5
15.4	7
17.46	9

Table 8. Summary of photocatalytic test results with 0.06 g catalyst.

Time(min)	Concentration (mg/L)	pH	Efficiency (%)
16	45	4	98.86
23	62.5	6	85.76
16	27	8	87.29
23	10	10	65.11
16	45	12	40.22

interaction between particles is the sum of the electrical double layer and the van der Waals interaction which is determined by the magnitude of the Hamaker constant of the material. Zeta potential is a measure of magnitude of charges on nanoparticles the higher the value (positive or negative), the more stable the colloid dispersion is normally a value >30 mV indicates good stability. Since the SrMGd(3%)/fGO showed the best results in different pH's, the variation of zeta potential vs. pH is presented in Table 7 and can be concluded the highest stability of the system occurred at pH=5.

Photocatalyst performance tests

The parameter of time, catalytic mass, and pH were reported in Table 8. After preparation, the solution was stirred for 1 h followed by centrifugation. It was then exposed to radiation. To this end, a cubic batch photoreactor was used which was equipped with 4 UV lamps 16W at each of its corners. The sample container was made of quartz and placed in the middle of the reactor to receive uniform UV radiation. After a determined time, the absorbance of the samples was read at the maximum wavelength of 278 nm using UV-Vis. spectrophotometer.

Factors affecting the catalytic performance

Factors affecting the catalytic performance:

To achieve the highest performance, DOE analysis was performed using affecting parameters. The summary of results is presented as follows:

Effect of pH and catalyst mass on drug removal efficiency:

Increase of the catalyst mass and reduction of pH enhanced the drug degradation efficiency

Effect of time and catalyst mass on drug degradation efficiency:

According to the results, the drug degradation efficiency incremented by prolonging the reaction time and catalyst mass to an acceptable level.

Effect of catalyst mass and drug concentration on drug degradation recovery:

According to the findings, drug degradation efficiency enhanced by increasing the catalyst mass and declining the drug concentration.

Optimal condition:

Based on the applied software (Minitab 16), the best point leading to the highest efficiency (99.98%) involves the following conditions: 0.06 g catalyst,

25.97 min reaction time, the concentration of 42.60 mg/L, and pH=5 (Fig 9).

CONCLUSIONS

This research reports the successful synthesis of $SrGd_xFe_{12-x}O_{19}$/GO-COOH composites and its characterization by various techniques. The results indicated that $SrGd_xFe_{12-x}O_{19}$/GO-COOH composite can be employed as an applicable candidate for the photodegradation of ENR antibiotic drug from the pharmaceutical industry effluent as well as the water resources. Analysis of the results by statistical software based on the response surface method showed that the prolongation of the radiation time and catalyst mass, as well as pH reduction, can enhance the efficiency of ENR photodegradation. By increasing the pollutant concentration, however, the degradation efficiency declined. The results also suggest that among the studied factors, pH had the highest impact on the ENR photodegradation efficiency. Finally, the software determined at the best point resulting in the optimal degradation efficiency (98.86%) which involved the following condition: 0.05 g catalyst, radiation time of 16 min, the concentration of 45 mg/L, and pH=4.

CONFLICT OF INTEREST

The authors declare no conflicts of interest.

REFERENCES

[1]. Qiu W, Zheng M, Sun J, Tian Y, Fang M, Zheng Y, Zhang T,Zheng C, Photolysis of Enrofloxacin, Pefloxacin and Sulfaquinoxaline in Aqueous Solution by UV/H2O 2, UV/Fe(II), and UV/H 2 O 2/Fe(II) and the Toxicity of the Final Reaction Solutions on Zebrafish Embryos, Science of The Total Environment, 651 (2019) 1457-1468. https://doi.org/10.1016/j.scitotenv.2018.09.315

[2]. Homem V,Santos L, Degradation and removal methods of antibiotics from aqueous matrices - A review, Journal of environmental management, 92 (2011). 2304-2347. https://doi.org/10.1016/j.jenvman.2011.05.023

[3]. Liu JL, Wong MH. Pharmaceuticals and personal care products (PPCPs): a review on environmental contamination in China. Environ Int. 2013;59:208-224. https://doi.org/10.1016/j.envint.2013.06.012

[4]. Huang W, Liu N, Zhang X, Wu M,Tang L, Metal organic framework g-C3N4/MIL-53(Fe) heterojunctions with enhanced photocatalytic activity for Cr(VI) reduction under visible light, Applied Surface Science. 425 (2017) 107-116. https://doi.org/10.1016/j.apsusc.2017.07.050

[5]. Tang L, Wang J-j, Jia C-t, Lv G-x, Xu G, Li W-t, Wang L, Zhang J-y,Wu M-h, Simulated solar driven catalytic degradation of psychiatric drug carbamazepine with binary BiVO4 heterostructures sensitized by graphene quantum dots, Applied Catalysis B: Environmental.205 (2017) 587-596. https://doi.org/10.1016/j.apcatb.2016.10.067

[6]. Lima, Veronica B., Lorena A. Goulart, Robson S. Rocha, Juliana R. Steter, and Marcos RV Lanza. "Degradation of antibiotic ciprofloxacin by different AOP systems using electrochemically generated hydrogenperoxide."Chemosphere (2020): 125807. https://doi.org/10.1016/j.chemosphere.2019.125807

[7]. Kamranifar M, Allahresani A,Naghizadeh A. Synthesis and characterizations of a novel CoFe2O4@ CuS magnetic nanocomposite and investigation of its efficiency for photocatalytic degradation of penicillin G antibiotic in simulated wastewater, Journal of Hazardous Materials, 366 (2019) 545-555 https://doi.org/10.1016/j.jhazmat.2018.12.046

[8]. Sayadi M H, Sobhani S,Shekari H, hotocatalytic degradation of azithromycin using GO@Fe3O4/ ZnO/ SnO2 nanocomposites. Journal of Cleaner Production. Journal of Cleaner Production.232 (2019) https://doi.org/10.1016/j.jclepro.2019.05.338

[9]. Wang Y, Tian D, Chu W, Li M,Lu X, Nanoscaled magnetic CuFe2O4 as an activator of peroxymonosulfate for the degradation of antibiotics enorfloxacin, Separation and Purification Technology, 212 (2019) 536-544. https://doi.org/10.1016/j.seppur.2018.11.051

[10]. Dhiman P, Dhiman N, Kumar A, Sharma G, Naushad M,Ghfar A A, Solar active nano-Zn1–xMgxFe2O4 as a magnetically separable sustainable photocatalyst for degradation of sulfadiazine antibiotic, Journal of Molecular Liquids, 294 (2019) https://doi.org/10.1016/j.molliq.2019.111574

[11]. Palomares-Sánchez S, Castro M G,Castañeda S P, Engineering Magnetic, Lead Hexaferrite - A Brief Review, Materials Research Foundations, Dielectric and Microwave Properties of Ceramics and Alloys, 57 (2019) 23-56. DOI: https://doi.org/10.21741/9781644900390-2

[12]. Pullar R C, Hexagonal ferrites: A review of the synthesis, properties and applications of hexaferrite ceramics, Progress in Materials Science, 57 (2012) 1191-https://doi.org/10.1016/j.pmatsci.2012.04.001

[13]. Sahoo J K, Konar M, Rath J, Kumar D,Sahoo H, Synthesis, Characterization and Dye Adsorption Performance of Strontium Ferrite decorated Bentonite-CoNiAl Magnetic Composite. 0Separation Science and Technology.55 (2020). https://doi.org/10.1007/s13369-020-04544.

[14]. Yousefi M, Afghahi S, Amini M,Torbati M B, An investigation of structural and magnetic properties of Ce-Nd doped strontium hexaferrite nanoparticles as a microwave absorbent ",Materials Chemistry and Physics 235 (2019) 121722-121738. https://doi.org/10.1016/j.matchemphys.2019.121722

[15]. Veisi S S, Yousefi M, Amini M, Shakeri A,Bagherzadeh M, Magnetic and microwave absorption properties of Cu/Zr doped M-type Ba/Sr hexaferrites prepared via sol-gel auto-combustion method, Journal of Alloys and Compounds.773 (2019) 1187-1194. https://doi.org/10.1016/j.jallcom.2018.09.189

[16]. Bañuelos-Frías A, Martínez-Guajardo G, Alvarado-Perea L, Canizalez-Dávalos L, Ruiz F,Valero-Luna C, Light absorption properties of mesoporous barium hexaferrite, BaFe12O19, Materials Letters, 252 (2019) 239-243. https://doi.org/10.1016/j.matlet.2019.05.137

[17]. Xu, Yuanguo, Feiyue Ge, Meng Xie, Shuquan Huang, Junchao

Qian, Hefei Wang, Minqiang He, Hui Xu, and Huaming Li. "Fabrication of magnetic BaFe 12 O 19/Ag 3 PO 4 composites with an in situ photo-Fenton-like reaction for enhancing reactive oxygen species under visible light irradiation." Catalysis Science & Technology 9, no. 10 (2019): 2563-2570 https://doi.org/10.1039/C8CY02449A

[18]. Mahdiani M, Sobhani A,Salavati-Niasari M The first synthesis of CdFe12O19 nanostructures and nanocomposites and considering of magnetic, optical, electrochemical and photocatalytic properties, Journal of Hazardous Materials, 367 (2019) 607-619 https://doi.org/10.1016/j.jhazmat.2019.01.007

[19]. Mahdiani M, Soofivand F, Ansari F,Salavati-Niasari M Maryam Mahdiani, Faezeh Soofivand, Fatemeh Ansari, Masoud Salavati-Niasari, Grafting of CuFe12O19 nanoparticles on CNT and graphene: Eco-friendly synthesis, characterization and photocatalytic activity, Journal of Cleaner Production, 176 (2018) 1185-1197. https://doi.org/10.1016/j.jclepro.2017.11.177

[20]. Mohanta O, Singhbabu Y, Giri S, Dadhich D, Das N,Sahu R K Degradation of Congo red pollutants using microwave derived SrFe12O19: An efficient magnetic photocatalyst under visible light, Journal of Alloys and Compounds,564 (2013) 78 - 83. https://doi.org/10.1016/j.jallcom.2013.02.074

[21]. Kar M K A, Fazaeli R, Manteghi F,Ghahari M , Environmental Progress & Sustainable Energy, Structural, Optical, and Isothermic Studies of CuFe2O4 and Zn-Doped CuFe2O4 Nanoferrite as a Magnetic Catalyst for Photocatalytic Degradation of Direct Red 264 Under Visible Light Irradiation 38 (2019) 13109. https://doi.org/10.1002/ep.13109

[22]. Kaur P, Kaushik A,Singhal S Paramdeep Kaur, Anupama Kaushik, Sonal Singhal, Comparative evaluation of photocatalytic performance of hexagonal ferrites procured via sol-gel route, Materials Today: Proceedings, 14 (2019) 426-434. https://doi.org/10.1016/j.matpr.2019.04.165

[23]. Al-Garalleh G A, Mahmood S H, Bsoul I,Loloee R, Structural and magnetic properties of RE-Al substituted nanocrystalline hexaferrites (Sr1−x RE x Al2Fe10O19), Materials Research Express, 7 (2020). https://doi.org/10.1088/2053-1591/ab5ddd

[24]. Almessiere M, Slimani Y,Baykal A Magneto-optical properties of rare earth metals substituted Co-Zn spinel nanoferrites, Ceramics International, 45 (3)(2019) 3449-3458. https://doi.org/10.1016/j.ceramint.2018.10.260

[25].Ahmadi M, Kazeminejad I, Iranian Journal of Crystallography and Mineralogy, 27 (2019)245-254, https://doi.org/10.29252/ijcm.27.1.245

[26]. Ali I, Islam M, Awan M,Ahmad M Effects of Ga-Cr substitution on structural and magnetic properties of hexaferrite (BaFe12O19) synthesized by sol-gel auto-combustion route, Journal of Alloys and Compounds, 547 (2013) 118-125. https://doi.org/10.1016/j.jallcom.2012.08.122

[27]. Vinnik D, Klygach D, Zhivulin V, Malkin A, Vakhitov M, Gudkova S, Galimov D, Zherebtsov D, Trofimov E,Knyazev N, Electromagnetic properties of BaFe12O19:Ti at centimeter wavelengths, Journal of Alloys and Compounds.755 (2018) 177-183. https://doi.org/10.1016/j.jallcom.2018.04.315

[28]. Trukhanov A, Kostishyn V, Panina L, Korovushkin V, Turchenko V, Thakur P, Thakur A, Yang Y, Vinnik D,Yakovenko Em 754 Control of electromagnetic properties in substituted M-type hexagonal ferrites, 2018 Journal of Alloys and Compounds, 754 (2018) 247-256. https://doi.org/10.1016/j.jallcom.2018.04.150

[29]. Yang Y, Wang F, Shao J, Huang D, He H, Trukhanov A,Trukhanov S Influence of Nd-NbZn co-substitution on structural, spectral and magnetic properties of M-type calcium-strontium hexaferrites Ca0.4Sr0.6-xNdxFe12.0-x(Nb0.5Zn0.5)xO19, Journal of Alloys and Compounds, 765 (2018) 616-623. https://doi.org/10.1016/j.jallcom.2018.06.255

[30]. Hessien M, El-Bagoury N, Mahmoud M, Alsawat M, Alanazi A K,Rashad M, Implementation of La3+ ion substituted M-type strontium hexaferrite powders for enhancement of magnetic properties, Journal of Magnetism and Magnetic Materials, 498 (2020) 0304-8853. https://doi.org/10.1016/j.jmmm.2019.166187

[31]. Cernea M, Greculeasa S G, Radu R, Aldica G, Ganea P, Surdu V A, Tanasa E, Cioangher M, Iacob N,Costescu R M, Magnetic properties of BaNixFe12-xO19 (x=0.0-1.0) hexaferrites, synthesized by citrate-gel auto-combustion and sintered by conventional and spark plasma methods Journal of Alloys and Compounds (2020) Journal pre-Proof, https://doi.org/10.1016/j.jallcom.2020.154850

[32]. Kar M K A, Fazaeli R, Manteghi F,Ghahari M, Environmental Progress & Sustainable Energy.38 (2019) Elimination of direct red 264 using magnetic pure and Zn-doped NiFe2O4 nanophotocatalysts under visible light irradiation: Isothermic and kinetic studies 38(2019)13097. https://doi.org/10.1002/ep.13097

[33]. Liaquat A, Anis-ur-Rehman M,ul Haq A Impact of Gd doping on the dielectric and magnetic properties of (Sr-Ba) Fe12O19 nanoparticles, Journal of Alloys and Compounds, 822 (2020) 153561. https://doi.org/10.1016/j.jallcom.2019.153561

[34]. Abdollahi F, Yousefi M, Hekmati M, Khajehnezhad A, Afghahi S,Salman S , Magnetic and microwave absorption properties of barium hexaferrite doped with La3+ and Gd3+, Journal of Nanostructures, 9 (2019). https://doi.org/10.22052/JNS.2019.03.019

[35]. Wu Z, Zhang R, Yu Z, Shan L, Dong L,Zhang X, Study on preparation and magnetic properties of Sr1−xGdxFe12−xCuxO19 (0.00 ≤ x ≤ 0.20) strontium ferrite prepared by solid phase method. Ferroelectrics 523(2018) 82-88. https://doi.org/10.1080/00150193.2018.1391569

[36]. Luo J, Yue L, Ji H, Zhang K,Yu N Investigation on the optimization, design and microwave absorption properties of BaTb0.2Eu0.2F.e11.6O19/PANI decorated on reduced graphene oxide nanocomposites, Journal of materials science, 54 (2019) 6332-6346. https://doi.org/10.1007/s10853-018-03305-7

[37]. Zhang K, Luo J, Yu N, Gu M,Sun X, Synthesis and excellent electromagnetic absorption properties of reduced graphene oxide/PANI/BaNd0.2Sm0.2Fe11.6O19 nanocomposites, , Journal of Alloys and Compounds, 779 (2019) 270-279. https://doi.org/10.1016/j.jallcom.2018.11.284

[38]. Afghahi S S S, Jafarian M,Atassi Y, Microstructural and magnetic studies on BaMgxZnxX2xFe 12−4x O19 (X=Zr,Ce,Sn) prepared via mechanical activation method to act as a microwave absorber in X-band, Journal of Magnetism and Magnetic Materials, 406 (2016) 184-191. https://doi.org/10.1016/j.jmmm.2016.01.020

[39]. Davoodi A,Hashemi B, Magnetic properties of Sn-Mg substituted strontium hexaferrite nanoparticles synthesized via coprecipitation method, Journal of Alloys and Compounds, 509 (2011) 5893-5896. https://doi.org/10.1016/j.jallcom.2011.03.002

[40]. Huang, Jiaxing, Daguang Li, Ruobai Li, Ping Chen, Qianxin Zhang, Haijin Liu, Wenying Lv, Guoguang Liu, and Yiping Feng. "One-step synthesis of phosphorus/oxygen co-doped g-C3N4/anatase TiO2 Z-scheme photocatalyst for significantly enhanced visible-light photocatalysis degradation of enrofloxacin." Journal of hazardous materials 386 (2020): 121634. https://doi.org/10.1016/j.jhazmat.2019.121634